Available online at www.sciencedirect.com
ScienceDirect
Journal of Power Sources 177 (2008) 303–313
JOURNAL OF POWER SOURCES
www.elsevier.com/locate/jpowsour

Comparison between numerical simulation and visualization experiment on water behavior in single straight flow channel polymer electrolyte fuel cells

Hiromitsu Masuda [1], Kohei Ito *, Toshihiro Oshima [2], Kazunari Sasaki [3]

Kyushu University, Faculty of Engineering, Department of Mechanical Engineering Science, Motooka 744, Nishi-ku, Fukuoka-shi, Fukuoka 819-0395, Japan

Received 21 August 2007; received in revised form 13 November 2007; accepted 14 November 2007
Available online 11 January 2008

Abstract

A relationship between a flooding and a cell voltage drop for polymer electrolyte fuel cell was investigated experimentally and numerically. A visualization cell, which has single straight gas flow channel (GFC) and observation window, was fabricated to visualize the flooding in GFC. We ran the cell with changing operation condition, and measured the time evolution of cell voltage and took the images of cathode GFC. Considering the operation condition, we executed a developed numerical simulation, which is based on multiphase mixture model with a formulation on water transport through the surface of polymer electrolyte membrane and the interface of gas diffusion layer/GFC. As a result in experiment, we found that the cell voltage decreased with time and this decrease was accelerated by larger current and smaller air flow rate. Our simulation succeeded to demonstrate this trend of cell voltage. In experiment, we also found that the water flushing in GFC caused an immediate voltage change, resulting in voltage recovery or electricity generation stop. Although our simulation could not replicate this immediate voltage change, the supersaturated area obtained by our simulation well corresponded to fogging area appeared on the window surface in the GFC.

Keywords: Polymer electrolyte fuel cell; Flooding; Visualization; Numerical simulation; Two-phase flow

1. Introduction

Water management, to control the water transport to avoid dehydration and flooding, is critical issue to improve the performance of polymer electrolyte fuel cell (PEFC). Operating PEFC under high current density and/or low Stoichiometric condition often invites the flooding, which forms locally and spreads in the cell. Once the flooding starts, the reactants gas supply to catalyst layer is blocked, and then the cell performance deteriorates accompanying with increase of concentration overpotential. To improve the performance of PEFC, understanding the mechanism of the water transport in cell is required as first step, and then the proper design and the optimization of operation condition should be established.

The flooding appears in every segment in cell, such as gas flow channel (GFC), gas diffusion layer (GDL) and catalyst layer (CL). The flooding in GFC was observed with visualization cell, whose separator partially made with transparent material such as glass [1,2]. In addition to the visualization in GFC, recent neutron imaging technique [3] enables us to visualize whole region in cell. Though it is generally difficult to visualize the flooding in GDL, which is characterized as micro-porous and opaque material, neutron beam property and advanced spectroscopy technology enable us to visualize every segment in cell.

The numerical simulation of flooding in PEFC has been also progressed. Based on the multiphase mixture model [4], a lot of two-phase flow simulations of PEFC have been reported: a simulation which turns its attention especially to cathode channel and GDL [5]: a simulation explicitly considering catalytic layer [6]: a simulation focused on the GDL under rib [7]: a simulation for transient response of unit-cell [8].

* Corresponding author. Tel.: +81 92 802 3144; fax: +81 92 802 0001.
E-mail addresses: masuda@mech.kyushu-u.ac.jp (H. Masuda), kohei@mech.kyushu-u.ac.jp (K. Ito), oshima@mech.kyushu-u.ac.jp (T. Oshima), sasaki@mech.kyushu-u.ac.jp (K. Sasaki).
[1] Tel.: +81 92 802 3095.
[2] Tel.: +81 92 802 3094.
[3] Tel.: +81 92 802 2735.

0378-7753/$ – see front matter © 2007 Elsevier B.V. All rights reserved.
doi:10.1016/j.jpowsour.2007.11.069

Nomenclature

A	area (m^2)
c	concentration ($mol\,m^{-3}$)
C	capacitance (F)
D	diffusion coefficient ($m^2\,s^{-1}$)
F	Faraday's constant ($C\,mol^{-}$)
i	current density ($A\,cm^{-2}$)
I	current (A)
k	permeability (m^2)
K	transport coefficient ($m\,s^{-1}$)
k_v	phase change rate constant ($1\,s^{-1}$)
m_{gl}	phase change rate ($kg\,(m^3\,s)^{-1}$)
n_d	electro-osmotic coefficient
P	pressure (Pa)
Q	electric charge (C)
R	gas constant or resistance ($J\,(mol\,K)^{-1}$ or Ω)
s	liquid water saturation
T	temperature (K)
$\mathbf{u}$	velocity vector ($m\,s^{-1}$)
V	volume or cell voltage (m^3 or V)
Y	mass fraction

Greek symbols

δ	thickness (μm)
ε	porosity
η	overpotential (V)
λ	relative mobility
μ	viscosity (Pa s)
ν	kinematic viscosity ($m^2\,s^{-}$)
θ_c	contact angle (°)
ρ	density ($kg^{-}m^{-3}$)
σ	surface tension or proton conductivity ($N\,m^{-1}$ or $S\,m^{-1}$)
τ	tortuosity
ξ	utilization ratio

Subscripts

ano	anode
act	active
BV	Butler–Volmer
c	capillary
cat	cathode
eff	effective
eq	equilibrium state
g	gas phase
gdl	gas diffusion layer
gfc	gas flow channel
l	liquid phase
m	membrane
OC	open circuit
ohm	Ohmic
rep	representative
sat	saturation

Superscripts

H_2	hydrogen
H_2O	water
I	gas species
liq	liquid
O_2	oxygen
p	pore
vap	vapor
w	water

Thus the both of visualization experiment and numerical simulation for the flooding have been progressed. However, precise cross comparison between them does not seem to have been done. Almost numerical studies have been evaluated only by the comparison with the measured current–voltage characteristics, which is categorized as whole and steady state characteristics. Liquid water saturation and its time evolution has not been compared between simulation and visualization study.

On the basis of this background, a simple visualization cell, which has single straight GFC, was fabricated to precisely compare numerical result with the visualized flooding images in GFC. We ran the cell with changing operation condition, and measured the time evolution of cell voltage in addition to successively recording the visualized image in GFC. Considering the geometry of the cell and the operation condition, we executed a developed numerical simulation, which is based on Multiphase mixture model with the punctilious formulation on water transport through the polymer electrolyte membrane (PEM)/GDL and the GDL/GFC interface. And then we evaluated the numerical simulation result by the comparison with the visualization experiment result. In the following, the visualization experiment method and the formulation used in the simulation are explained. Subsequently experimental result and numerical simulation result are shown.

2. Experimental method

2.1. Cell specification

To investigate the liquid water behavior in GFC, a simple visualization cell, which has single straight GFC, was fabricated as shown in Fig. 1. Comparing typical cell such as serpentine and parallel flow channel cell, our simple cell has advantages: we can directly analyze the relationship between flooding and cell voltage without additional consideration such as water transport under rib appeared in typical cell: the cell geometry can be easily incorporated into numerical simulation.

Fig. 1 shows top and side view of the visualization cell. Separators and back-plates were made of SUS316, and the separators were gilded to reduce electric contact resistance and to protect separators from corrosion. A rectangular GFC was formed, and its width, depth and length are 1.6, 1.0 and 30 mm, respectively. The geometry and the size of anode channel are as same as that of cathode channel. We used Gore PRIMEA® membrane-electrode assembly (Series 5510, electrolyte membrane thickness: 30 μm,

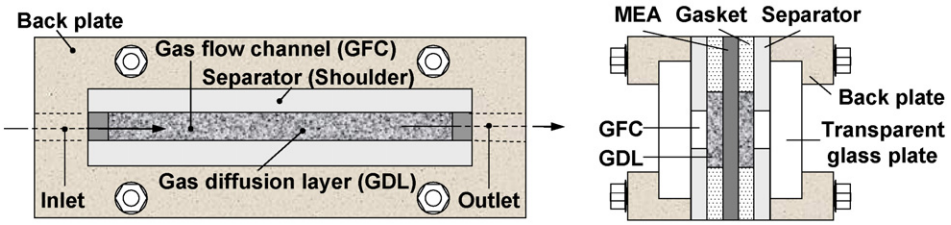

Fig. 1. Top and side view of visualization cell.

Table 1
Dimension of visualization cell

Quantity	Value
Width of GFC (mm)	1.6
Depth of GFC (mm)	1
Length of GFC (mm)	30
Width of GDL (mm)	3.2
Thickness of GDL (μm)	300
Length of GDL (mm)	30
Active area (cm^2)	0.96
Thickness of PEM (μm)	30

catalyst loading of anode and cathode: 0.3 mg cm^{-2}), which was sandwiched between two sheets of GDL (CARBEL-CL®, carbon cloth type). GDL was cut as 3.2 mm × 30 mm so that it covers GFC area. We assume that this GDL area of 0.96 cm^2 determines the effective active area. Other dimensions of the cell are listed in Table 1.

2.2. Test bench for cell

Fig. 2 is the cell test bench, which consists of the control system of gases flow, temperature and electricity. The reactant gas for cathode was air, and that for anode was hydrogen. Mass flow controller (CMQ-V, YAMATAKE) regulated gases flow rate. Both anode and cathode gas were humidified with the bubbler, whose temperature was controlled by water bath. The separator and the ambient of cell were kept at constant temperature. The visualized image in GFC was recorded through transparent window of cell with microscope (VHX-200, KEYENCE). AC impedance (1280B, Solatron) was also recorded intermittently to grasp Ohmic and activation overpotential.

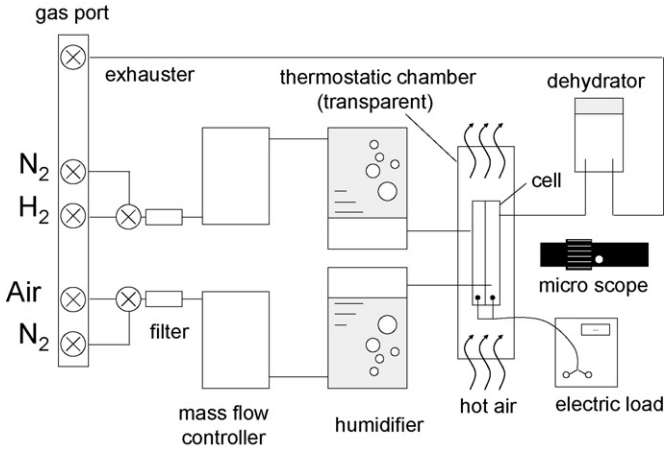

Fig. 2. Test bench for cell operation.

Table 2
Operation conditions

Number	Current (A)	Air flow (sccm)	H_2 flow (sccm)	Utilization ratio
1-1	0.15	58	22	0.05
1-2	0.15	116	46	0.025
1-3	0.15	232	92	0.0125
2-1	0.3	58	22	0.1
2-2	0.3	116	46	0.05
2-3	0.3	232	92	0.025
3-1	0.6	58	22	0.2
3-2	0.6	116	46	0.1
3-3	0.6	232	92	0.05

Cell temperature (°C): 30, inlet relative humidity (%): 75.

2.3. Operation conditions

A main purpose of our experiment is to observe flooding in GFC under a given operation condition, and then try to understand the impact of the flooding on cell voltage. The cell temperature was controlled to be 30 °C, which is considered to be rather low. This low cell temperature, however, allows us to observe flooding phenomena efficiently, because lower temperature promotes to condense water vapor produced by cathode reaction. The relative humidity of reactant gases at GFC inlet was controlled to be 75%. Other operation conditions such as load current density and flow rate are listed in Table 2. Our simple cell was somewhat unstable. So we chose rather high utilization ratio in this experiment. The visualized image in GFC with microscope was recorded at every 15 s.

Comparing with practical operation condition, the cell temperature and the utilization ratio in this study are low and high, respectively. However, it is thought that our result is still helpful for the practical case. The water behavior, which is shown in the later section and denoted as flooding and flushing, also appears under practical condition. Water transport in our case is thought to be essentially same as practical case. All we have to pay attention is the nature that lower temperature and the smaller utilization work to accelerate water production and water drainage, respectively.

3. Mathematical model

The simulation domain is shown in Fig. 3. A unit-cell with single straight GFC is numerically simulated as two-dimensional field. The simulation domain includes GFC, GDL and PEM. The multiphase mixture model [4] was used for two-phase flow formulation in GDL, and Stefan–Maxwell equation [9] is used for multi-component diffusion. The equivalent electric circuit

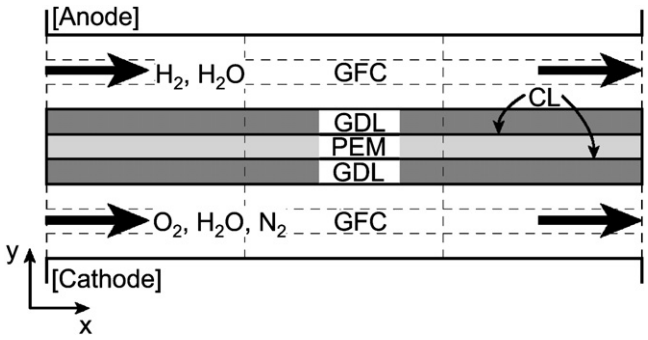

Fig. 3. Calculation domain. Mass, momentum and electric transport is treated to be two-dimensional.

[10] shown in Fig. 4 was employed to calculate the cell voltage, overpotentials and current distribution. Our simulation used the following assumptions: (i) CL is assumed to be infinitely thin and the cell reaction occurs at the interface between PEM and GDL, (ii) cell temperature is constant and uniform, (iii) transport property of GDL is isotropic.

Simulation with the assumption about constant and uniform temperature might lead to the overestimation of water saturation. Especially for higher current density condition, this overestimation of water saturation is thought to be promoted considering that the high current increases temperature and saturation vapor pressure. However qualitative impact of load current and flow rate on water behavior can be simulated at least, even if the constant and uniform temperature are assumed. This point is reinforced by the correspondence between simulation and experiment as shown in the later section.

3.1. Governing equations

The governing equations used here followed our previous study [8] and the reference of [4,9,10]. In the equations, liquid water saturation of s was used as key variable, which is defined as the ratio of liquid water volume to pore volume:

$$s = \frac{V_\mathrm{l}}{V_\mathrm{p}} \tag{1}$$

Continuity equation for gas and liquid mixture in GDL and GFC is,

$$\frac{\partial}{\partial t}(\varepsilon^* \rho) + \nabla \cdot (\rho \mathbf{u}) = 0 \tag{2}$$

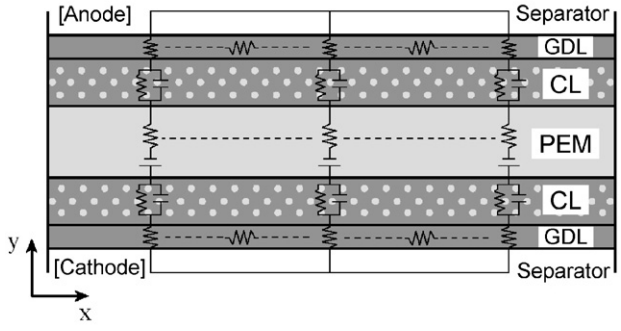

Fig. 4. Equivalent electrical circuit.

Table 3
Source terms in governing equations in GFC and GDL

	S_u	S_i
Channel	0	$-\varepsilon^* m_\mathrm{gl}$ (i = vapor)
GDL	$-\frac{\nu}{K}\rho\varepsilon^* \mathbf{u}$	0 (i = H_2, O_2)

Here, ρ is the density of two-phase mixture defined as,

$$\rho = (1-s)\rho_\mathrm{g} + s\rho_\mathrm{l} \tag{3}$$

Momentum conservation equation for the mixture in GDL and GFC is,

$$\frac{\partial}{\partial t}\left(\frac{1}{\varepsilon^*}\rho\mathbf{u}\right) + \nabla \cdot \left(\frac{1}{\varepsilon^{*2}}\rho\mathbf{u}\mathbf{u}\right) = -\nabla P + \nabla \cdot \left[\nu \nabla \cdot \left(\frac{1}{\varepsilon^*}\rho\mathbf{u}\right)\right] + S_\mathrm{u} \tag{4}$$

The last term of RHS, which can be treated as source term, means Darcy flow. In GDL and GFC region, mass conservation equation of gas species is,

$$\frac{\partial}{\partial t}\left[\varepsilon^*(1-s)\rho_\mathrm{g} y^i\right] = -\nabla \cdot \left[(1-s)\rho_\mathrm{g} y^i \mathbf{u}_\mathrm{g}\right] - \nabla \mathbf{j}_\mathrm{g}^i + S_i \tag{5}$$

and that of liquid phase is,

$$\frac{\partial}{\partial t}[\varepsilon^* \rho_\mathrm{l} s] + \nabla \cdot [\rho_\mathrm{l} \mathbf{u}_\mathrm{l} s] = \varepsilon^* m_\mathrm{gl} \tag{6}$$

Mass conservation for water in PEM is,

$$\frac{\partial \rho_\mathrm{m}^\mathrm{w}}{\partial t} = \nabla \cdot (D_\mathrm{m} \nabla \rho_\mathrm{m}^\mathrm{w}) + n_\mathrm{d} \frac{i}{F} M^{\mathrm{H_2O}} \tag{7}$$

The effective porosity of GDL denoted as $\varepsilon^*(=\varepsilon/\tau)$ used in above equations becomes unity in case of GFC. The source terms of S shown in Eqs. (4) and (5) are listed in Table 3.

3.2. Constitutive relations

3.2.1. Diffusive flux of multi-component

Diffusive flux of multi-component J_g in Eq. (5) is expressed as [9],

$$\begin{pmatrix} \mathbf{J}_\mathrm{g}^1 \\ \mathbf{J}_\mathrm{g}^2 \end{pmatrix} = -c_\mathrm{g} \begin{pmatrix} d_{11} & d_{12} \\ d_{21} & d_{22} \end{pmatrix} \begin{pmatrix} \nabla x^1 \\ \nabla x^2 \end{pmatrix}$$
$$\beta = x^1 D_\mathrm{eff}^{23} + x^2 D_\mathrm{eff}^{13} + x^3 D_\mathrm{eff}^{12},$$
$$d_{11} = \frac{D_\mathrm{eff}^{13}(x^1 D_\mathrm{eff}^{23} + (1-x^1) D_\mathrm{eff}^{12})}{\beta},$$
$$d_{12} = \frac{x^1 D_\mathrm{eff}^{23}(D_\mathrm{eff}^{13} - D_\mathrm{eff}^{12})}{\beta}$$
$$d_{21} = \frac{x^2 D_\mathrm{eff}^{13}(D_\mathrm{eff}^{23} - D_\mathrm{eff}^{12})}{\beta},$$
$$d_{22} = \frac{D_\mathrm{eff}^{23}(x^2 D_\mathrm{eff}^{13} + (1-x^2) D_\mathrm{eff}^{12})}{\beta} \tag{8}$$

where D_{eff} and c_{g} are the effective gas diffusion coefficient and the molar concentration of gas mixture defined respectively as,

$$D_{\text{eff}}^{ij} = \varepsilon^{*}(1-s)^{1.5} D_{\text{g}}^{ij} \tag{9}$$

$$c_{\text{g}} = \frac{P_{\text{g}}}{RT} \tag{10}$$

This gas pressure of P_{g} can be obtained from the multiphase mixture model [4], as rather difficult function of saturation of s through capillary pressure:

$$P_{\text{g}} = P + \int_0^s \frac{k_{\text{rl}}}{\nu_{\text{l}}} \nu \frac{\partial P_{\text{c}}}{\partial s} \mathrm{d}s \tag{11}$$

3.2.2. Supplemental relations and mixture properties [4]

In GDL of porous media, the gas and the liquid phase velocities denoted as $\mathbf{u}_{\text{l}}$ and $\mathbf{u}_{\text{g}}$ are expressed in the following.

$$\begin{aligned} \rho_{\text{g}}\mathbf{u}_{\text{g}} &= -\mathbf{j}_{\text{l}} + \lambda_{\text{g}}\rho\mathbf{u} \\ \rho_{\text{l}}\mathbf{u}_{\text{l}} &= \mathbf{j}_{\text{l}} + \lambda_{\text{l}}\rho\mathbf{u} \end{aligned} \tag{12}$$

In GFC, we assume that the two-phase flow is well mixed: the gas phase velocity is equal to liquid phase velocity. The capillary flux $\mathbf{j}_{\text{l}}$ can be expressed as,

$$\mathbf{j}_{\text{l}} = \frac{\lambda_{\text{l}}\lambda_{\text{g}}K}{\nu} \nabla P_{\text{c}} \tag{13}$$

The capillary pressure P_{c} is given by,

$$P_{\text{c}} = P_{\text{g}} - P_{\text{l}} = \left(\frac{\varepsilon}{K}\right)^{0.5} \sigma \cos\theta_{\text{c}} J(s) \tag{14}$$

The Leverett's function of $J(s)$ takes the following form:

$$J(s) = \begin{cases} 1.417(1-s) - 2.12(1-s)^2 + 1.263(1-s)^3, & \theta_{\text{c}} \le 90^{\circ} \\ 1.417s - 2.12s^2 + 1.263s, & \theta_{\text{c}} > 90^{\circ} \end{cases} \tag{15}$$

The coefficients of mixture transport properties appeared in above equations are given as:

Relative permeability:

$$k_{\text{rl}} = s^3, k_{\text{rg}} = (1-s)^3 \tag{16}$$

Kinematic viscosity:

$$\nu = \frac{1}{(k_{\text{rl}}/\nu_{\text{l}}) + k_{\text{rg}}/\nu_{\text{g}}} \tag{17}$$

Relative mobility:

$$\lambda_{\text{l}} = \frac{k_{\text{rl}}}{\nu_{\text{l}}}\nu, \quad \lambda_{\text{g}} = 1 - \lambda_{\text{l}} \tag{18}$$

3.2.3. Phase change rate

The phase change rate m_{gl} in Eqs. (5) and (6) can be expressed as:

$$\begin{aligned} m_{\text{gl}} &= k_{\text{v}}(\rho^{\text{vap}} - \rho_{\text{sat}}^{\text{vap}}) f(s), \\ f(s) &= \begin{cases} 1-s, & \text{if } (\rho^{\text{vap}} - \rho_{\text{sat}}^{\text{vap}}) > 0 \\ s, & \text{if } (\rho^{\text{vap}} - \rho_{\text{sat}}^{\text{vap}}) < 0 \end{cases} \end{aligned} \tag{19}$$

where k_{v} is phase change rate [11]. This expression means that the phase change is progressed within finite rate and that it allows supersaturation state.

3.2.4. Equivalent electric circuit

We considered the equivalent electric circuit [10] shown in Fig. 4. The circuit elements are coupled with the gas species concentrations in GDL and with the water content in PEM, which are obtained by the conservation equations mentioned above. Solving this circuit by Kirchhoff's law, the distribution of cell voltage, overpotential and current density distribution are obtained.

Local cell voltage is calculated from the following equation.

$$V_{\text{cell}} = V_{\text{OC}} - IR_{\text{ohm}} + \eta_{\text{cat}} \tag{20}$$

Here, V_{oc} is the open circuit voltage and η_{cat} is the cathode activation overpotential. V_{oc} is calculated from following Nernst equation.

$$\begin{aligned} V_{\text{OC}} = {} & 1.229 - 8.456 \times 10^{-4}(T_{\text{cell}} - 298.15) \\ & + 4.308 \times 10^{-5} T_{\text{cell}} \ln\left(\frac{P_{\text{H}_2} P_{\text{O}_2}^{0.5}}{P_{\text{H}_2\text{O}}}\right) \end{aligned} \tag{21}$$

R_{ohm} is the Ohmic resistance, and it mainly consists of proton resistance in PEM. Therefore R_{ohm} can be obtained as the function of local proton electric conductivity, namely as the function of local water content in PEM:

$$R_{\text{ohm}} = \int_0^{\delta m} \frac{1}{\sigma_{\text{m}}(\rho_{\text{m}}^{\text{w}}) A_{\text{act}}} \mathrm{d}y \tag{22}$$

In equivalent electric circuit as shown in Fig. 4, the CL is denoted as a parallel circuit, which consists of electric double layer capacitor and nonlinear activation overpotential resistance. The electric charge accumulated at the capacitor is calculated from,

$$\frac{\partial Q}{\partial t} = (i - i_{\text{BV}}) A_{\text{act}} \tag{23}$$

where i is the local current density. The i_{BV} in this equation is the current through the nonlinear resistance, and it is calculated from a Butler–Volmer equation.

$$i_{\text{BV}} = (1-s)^2 i_{0\text{c}} \left(\frac{c^{\text{O}_2}}{c_{\text{rep}}}\right) \exp\left(\frac{0.5F|\eta_{\text{cat}}|}{RT}\right) \tag{24}$$

In steady state, the local current density corresponds to this current density of i_{BV}.

Cathode activation overpotential η_{cat} is given as:

$$\eta_{\text{cat}} = -\frac{Q_{\text{cat}}}{C_{\text{cat}}} \tag{25}$$

where C_{cat} is the capacitance of the electric double layer capacitor, which changes with water content at CL. Anode activation overpotential is neglected here, because it is enough small not to influence the current distribution.

3.3. Boundary conditions

At the inlet of GFC, constant concentration of each species and of flow rate is specified. The inlet velocity of GFC is defined as a function of representative current of I_{rep}. The inlet velocity for anode and cathode GFC are respectively,

$$u_{in,cat} = \frac{I_{rep}/(4F)}{\xi_{cat} c^{O_2} A_{gfc}}, \quad u_{in,ano} = \frac{I_{rep}/(2F)}{\xi_{ano} c^{H_2} A_{gfc}} \tag{26}$$

Where A_{cha} is the channel cross-section and ξ is the utilization ratio of reactant gases to the representative current.

At the outlet of GFC, it is assumed that the velocity, the concentration and the liquid saturation fields are fully developed, and their gradients are zero:

$$\frac{\partial \mathbf{u}}{\partial n} = 0, \quad \frac{\partial c^i}{\partial n} = 0, \quad \frac{\partial s}{\partial n} = 0 \tag{27}$$

where n is normal vector to the boundary surface. At the boundary between separator and GFC, non-slip and impermeable conditions are applied for the mixture of gas and liquid.

$$\mathbf{u} = 0, \quad \frac{\partial c^i}{\partial n} = 0, \quad \frac{\partial s}{\partial n} = 0, \quad \frac{\partial P}{\partial n} = 0 \tag{28}$$

At the boundary between GDL and PEM, non-slip and impermeable conditions are also applied for the mixture of gas and liquid.

$$\mathbf{u} = 0, \quad \frac{\partial P}{\partial n} = 0 \tag{29}$$

3.4. Water transport model at interface

To obtain father agreement between numerical solution and visualization result, we especially pay attention to the water transport at the PEM/GDL and the GDL/GFC interface. We consider the non-equilibrium water content in PEM near the PEM/GDL interface, and distinguish liquid water transport from vapor transport. Including these concerns, the expression of water flux is given with a modification of previous study of [12].

$$f_w = (1-s)k_{vap}\rho_{gdl}^{vap} - (1-s)k_{m,vap}\rho_m^w + sk_{liq}\rho_l - sk_{m,liq}\rho_m^w \tag{30}$$

The first term in RHS is the water vapor flux through PEM/GDL interface, which starts from the vapor phase in GDL. The second term is the counter flux to the first term. The third term and the forth term are liquid water flux from GDL and from PEM, respectively. The vapor flux coefficients of k_{vap} and $k_{m,\,vap}$ were given in [12]. The liquid flux coefficients of k_{liq} and $k_{m,liq}$ were estimated from Zawodzinski et al. [13]. The equilibrium water densities in PEM, in the cases that the GDL is filled with water vapor and with liquid water, are easily derived from Eq. (30):

$$\rho_m^w|_{vap,eq} = \frac{k_{vap}}{k_{m,vap}}\rho_{gdl}^{vap}, \quad \rho_m^w|_{liq,eq} = \frac{k_{liq}}{k_{m,liq}}\rho^{liq} \tag{31}$$

This $\rho^w|_{vap,eq}$ agrees with the value reported by Springer et al. [14] within 20%, meaning that Eq. (31) roughly covers the equilibrium state.

We also well consider the liquid water transport through GDL/GFC interface with the modification of the transport model driven by capillary pressure [11]. Liquid water flux from GDL to GFC is given as

$$\mathbf{j}_{lb} = -n_b \rho^{liq} \frac{K_l}{\mu_l} \left(-\frac{dP_c}{ds}\right) s\nabla s \tag{32}$$

In this equation, we added a variable of n_b and considered flow rate dependence of $\mathbf{j}_{lb}$ with this variable. With this modification, the numerical simulation in the present study seems to show the better agreement with measurement result. The derivative of $(-dP_c/ds)$ is treated as a constant value following the previous study [11], though it is given as the function of saturation of s in general.

3.5. Numerical procedure

All equations shown in this section, which are mass and momentum conservation equations, equivalent electric circuit, and supplemental relations, are coupled and solved numerically. The equations of continuity and momentum conservation equation are solved by the SIMPLE method [15]. Physical, electrochemical and transport properties for simulation are listed in Table 4.

4. Experimental results and discussion

In this section, we show cell voltage, and the visualized image of flooding in cathode GFC, and their time evolution. Based on these experimental results, we discuss the influence of operation condition on flooding and on cell voltage.

4.1. Influence of flow rate on flooding

Fig. 5 is time evolutions of cell voltage, under the same current density of 0.6 A cm^{-2}, with different flow rate of 58, 116 and 232 sccm, corresponding to the experimental condition of No. 3-1, 3-2 and 3-3 as shown in Table 2. Fig. 6 is the visualized images, which are taken during the cell operation under these three conditions. These figures, as a whole, indicate that the vapor pressure in the cell reached saturation pressure, and flooding area gradually spread in GFC, resulting in the reduction of cell voltage.

At the moment when the current was loaded from 0 to 0.6 A cm^{-2}, the cell voltage instantly dropped as shown in Fig. 5, and this instant voltage drop was enhanced by smaller flow rate. This flow rate dependence on the cell voltage might be caused by the shortage of oxygen: smaller flow rate leads to the shortage of oxygen at cathode CL, resulting in larger activation overpotential.

After the instant voltage drop, each trend of cell voltage showed relatively-slow decrease, and smaller flow rate invited higher decreasing rate. Smaller flow rate seems to deteriorate the drainage of liquid water in GDL and GFC, leading to the high

Table 4
Physical, electrochemical and transport properties

Description	Value	Reference
Anode/cathode pressure, P (atm)	1.0/1.0	
Contact angle of GDL, θ_c (°)	110	
Electro-osmotic coefficient, n_d	1.0	
Faraday constant, F (C mol^{-1})	96487	
Liquid water density, ρ_l (kg m^{-3})	995.7	
Permeability of GDL, K (m^2)	1.0×10^{-12}	
Surface tension, σ (N m^{-1})	0.0627	
Universal gas constant, R (J (mol K)$^{-1}$)	8.314	
Viscosity of liquid water, μ_l (Pas)	0.8×10^{-3}	
Water diffusivity in PEM, D_m (m^2 s^{-1})	1.5×10^{-6}	
Cathode exchange current density, i_{0c} (A cm^{-2})	0.0017	Measured
Liquid water transport coefficient between GDL/GFC, n_b	0.08 (Air 232 sccm) 0.04 (Air 116 sccm) 0.02 (Air 58 sccm)	Adjustable
$-dP_c/ds$, (Pa)	22.95	
Liquid water permeability, K_l (m^2)	1.1×10^{-13}	[11]
Phase change rate constant, $k\nu$ (1 s^{-1})	100	
Vapor transport coefficient from PEM to GDL, $k_{m,vap}$ (m s^{-1})	1.46×10^{-7}	[12]
Vapor transport coefficient from GDL to PEM, k_{vap} (m s^{-1})	1.58×10^{-3}	
Liquid transport coefficient from PEM to GDL, $k_{m,liq}$ (m s^{-1})	8.24×10^{-6}	Estimated from [13]
Liquid transport coefficient from GDL to PEM, k_{liq} (m s^{-1})	6.01×10^{-6}	
Effective porosity of GDL, $\varepsilon^*(=\varepsilon/\tau)$	0.21 (cathode) 0.09 (anode)	[16]

decreasing rate of cell voltage. In addition an immediate voltage change, which is described as a vertical line in Fig. 5, was also observed especially under smaller flow rate conditions (No. 3-3, 3-2). Thus the trends of cell voltage in our experiment were categorized into two types: the relatively-slow decrease and the immediate change.

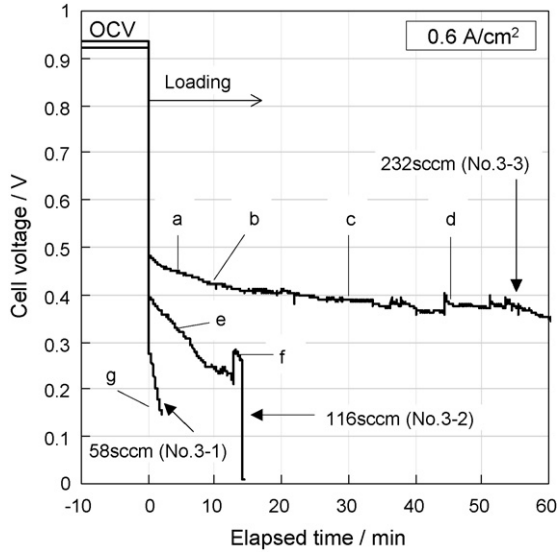

Fig. 5. Time variations of the cell voltage under the current condition of 0.6 A cm^{-2}, with the different air flow rate: 232 sccm (No. 3-3): 116 sccm (No. 3-2): 58 sccm (No. 3-1).

Fig. 6(a–d) are the successive image of water behavior in cathode GFC under 0.6 A cm^{-2} and 232 sccm condition (No. 3-3). After 5 min elapsed from applying load current, small water droplets began to appear near the outlet of GFC as shown in Fig. 6a, and the droplets almost popped up from the edge of GFC. Liquid water is thought to prefer to accumulate under the rib, where less convection is expected. It is noted that, despite experimental conditions, the point where water droplets pop up was exactly same. This means that the dominant path to flow liquid water exists in GDL, and that liquid water selectively migrates there.

After 10 min and 30 min elapsed, the water droplets grew, and combined near the outlet and at the midstream of GFC. In addition, the surface of glass was fogged partially. This fogged area might correspond to supersaturated area. After taking Fig. 6c, accumulated water flushed out of GFC, and the cell voltage immediately recovered by about 40 mV. Fig. 6d was taken just after this event, and it was found that the water droplets were cleaned off by the flushing. The above step-by-step events, namely the droplets popping-up, their growth, their combination and flushing, were observed repetitively, and it is thought to be one of the characteristic phenomena under a flooding condition.

Fig. 6e and f are the images under the 0.6 A cm^{-2} and 116 sccm condition (No. 3-2). Fig. 6e shows that water droplet growth under this condition was faster than that under 232 sccm condition (No. 3-1). Comparing between Fig. 6c and f, it can be seen that the more water in case of slower flow rate was accumulated in GFC even in shorter period. Just after Fig. 6f was taken, the accumulated water flushed. Different from the

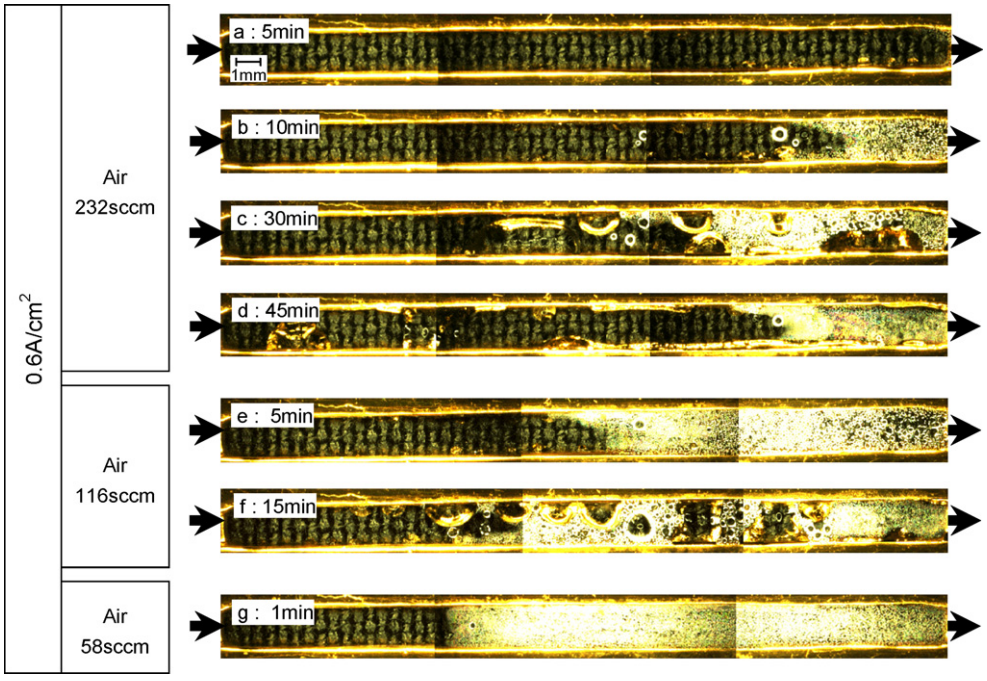

Fig. 6. Images of cathode GFC at the specified time, under the current condition of 0.6 A cm^{-2}, with the different air flow rate: 232 sccm (No. 3-3): 116 sccm (No. 3-2): 58 sccm (No. 3-1).

232 sccm condition, cell voltage immediately dropped, and electricity generation stopped after the flush. When this flushing happened, it was observed that something like water film covered the large area of GDL surface. It can be thought that this film triggered by the flushing fully clogged the pathway of oxygen gas supply to CL and invited the immediate voltage drop resulting in the electricity generated stop. The liquid film, mentioned just above, formed and disappeared within 1 s, and it emerged at irregular intervals. On the other hand the minimum intervals between recordings image is 15 s with the microscope used. This restriction invited the difficulty to record the image of liquid film. Regrettably we could not succeed to record the image of liquid film, although we caught it visually.

Fig. 6g is the image under the 0.6 A cm^{-2} and 58 sccm condition (No. 3-1). Under this smallest flow rate condition, the voltage decreasing rate was highest. After 2 min of operation, cell voltage decreased below 0.15 V and we stopped the operation. During this 2 min, no droplet was observed in GFC. This voltage drop did not seem to be caused by only a shortage of oxygen, because gas re-distribution after applying load current is estimated as to need only about 0.01 s. This representative time supports the explanation that the flooding in GDL and CL, which takes several minutes to develop, caused the voltage decreasing.

Summing up, it found that relatively-slow voltage decrease and the immediately voltage change are respectively caused by the flooding in porous media (GDL and CL) and by the flushing in GFC.

4.2. Influence of current on flooding

In this sub-section, the influence of load current on flooding is discussed by the experimental results of Figs. 7 and 8, under the same flow rate condition of 116 sccm, with the current density of 0.15, 0.3 and 0.6 A cm^{-2}, corresponding to the condition of No. 1-2, 2-2 and 3-2 shown in Table 2.

As a whole, it is found that a larger load current invited the wider flooding area and the higher decreasing rate of cell voltage. In the case of minimum current condition of 0.15 A cm^{-2}, the cell voltage almost kept constant, and the flooding in GFC was not developed. In the cases of larger current condition of 0.3 and 0.6 A cm^{-2}, the cell voltage kept decreasing, and the flooding was developed gradually. After the 14 and 36 min elapsed in

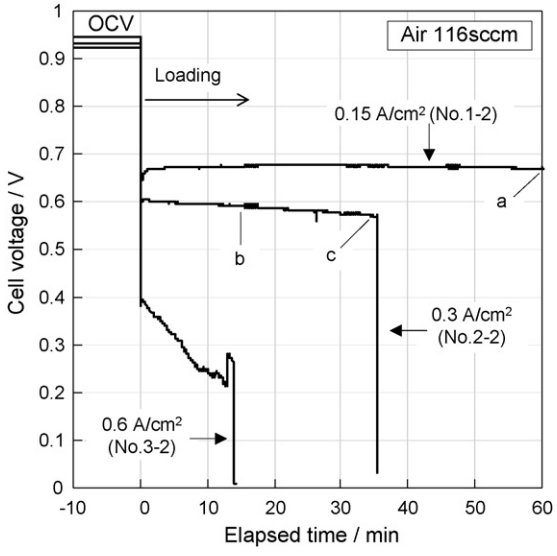

Fig. 7. Time variations of the cell voltage under the air flow rate condition of 116 sccm, with the different current: 0.6 A cm^{-2} (No. 3-2): 0.3 A cm^{-2} (No. 2-2): 0.15 A cm^{-2} (No. 1-2).

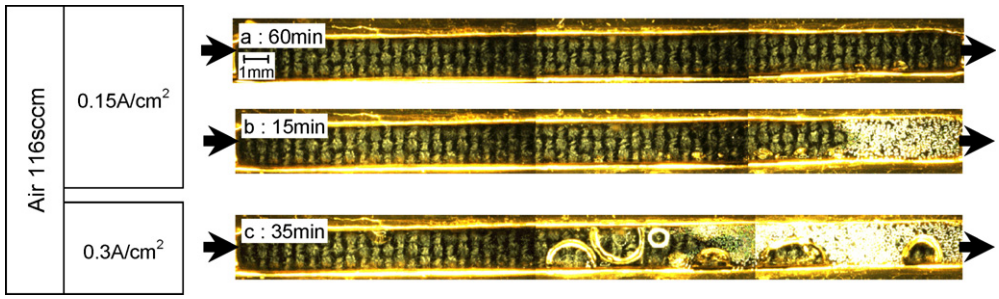

Fig. 8. Images of cathode GFC at the specified time, under the air flow rate condition of 116 sccm, with the different current: 0.3 A cm^{-2} (No. 2-2): 0.15 A cm^{-2} (No. 1-2).

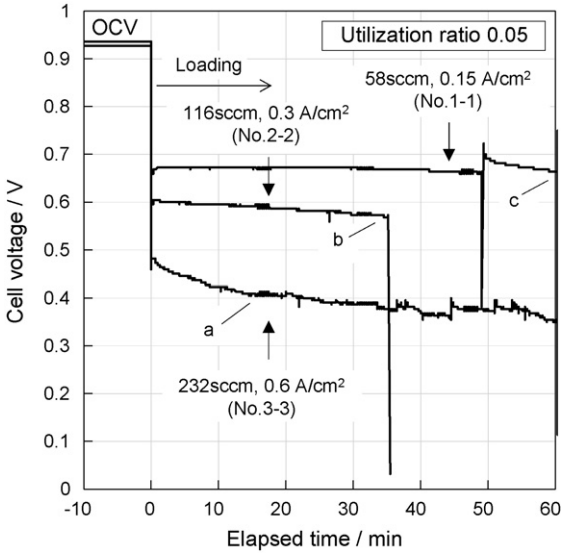

Fig. 9. Time variations of the cell voltage under the utilization ratio condition of 0.05, with the different current and air flow rate.

cases of these higher 0.3 and 0.6 A cm^{-2} condition respectively, the cell voltage dropped immediately and the electricity generation stopped with the flushing as also mentioned in Section 4.1, though the flooding did not fully covered the GDL surface as shown in Fig. 8. Thus it is understood that the flushing is a key event to cause the immediate generation stop.

4.3. Comparison of flooding between same utilization ratio conditions

In this sub-section, the flooding are compared between same utilization ratio conditions of 0.05 with changing load current and flow rate, whose experimental numbers are No. 1-1, 2-2, 3-3 as shown in Table 2. Contrary to our expectation, Figs. 9 and 10 indicate that the cell voltage under the highest current (largest flow rate) condition is stable rather than that under the lower current (smaller flow rate) condition. This could be caused by the effect that large flow rate enhance the drainage of water droplet in GFC. This flow rate effect is confirmed by the image of flooding in Fig. 10. Comparing the image between different flow conditions, the flooding area in case of the highest current (largest flow rate) condition is small, though the utilization ratio is same. Thus flow rate is one of key parameter to determine the degree of flooding.

The immediate voltage drops, shown in the case of No. 1-1 and 2-2 in Fig. 9, happened again after the flushing, being same fashion as shown in previous sections. After load current applied, water droplets popped up in GFC, and they accumulated there, and were flushed, resulting in the large voltage drop. On the other hand the cell voltage was rather stable in case of largest flow rate of No. 3-3. In this case water seems to be well balanced with repetitive accumulation and drainage.

5. Numerical simulation results and its comparison with experimental results

5.1. Time evolution of cell voltage

Fig. 11 shows the cell voltage change for nine cases of operation condition as listed in Table 2. Fig. 11a and b are the experimental and the simulation result, respectively. Different current density condition is indicated as dotted circle in the figures. For each current density condition, three voltage trends corresponding to three flow rate conditions are plotted. As a whole of the experimental result, the cell voltage was high under

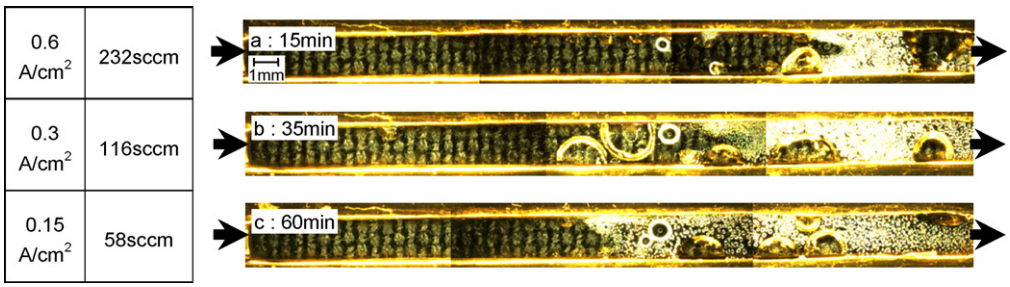

Fig. 10. Images of cathode GFC at the specified time, under the utilization ratio condition of 0.05, with the different current and air flow rate.

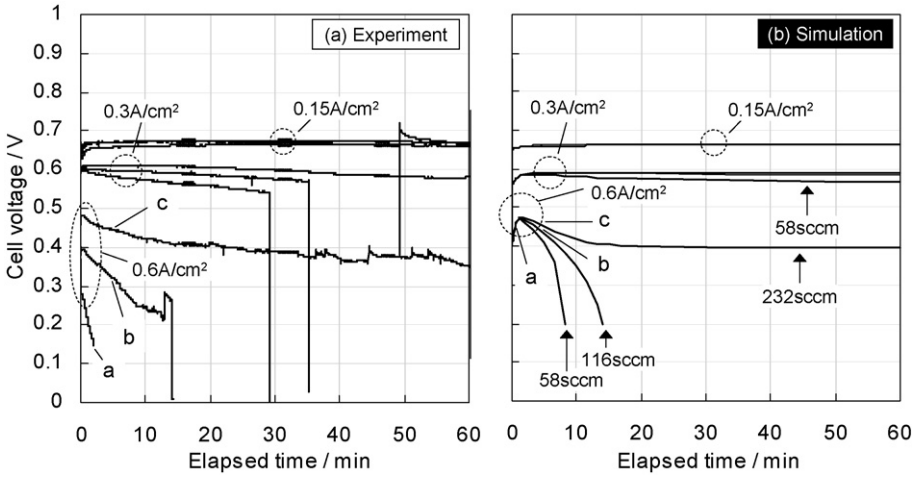

Fig. 11. Comparison of the cell voltage change between experiment and simulation. (a) Experimental results. (b) Simulation results.

lower current density and higher flow rate, although the flow rate dependence was rather obscure in cases of small current condition. Our simulation well predicts this overall trend of cell voltage change.

In case of 0.15 A cm^{-2} of the experimental result, cell voltage kept high, and flow rate dependence of it was small. The simulation result agreed with the experimental result.

In case 0.3 A cm^{-2}, experimental results showed that the cell voltage slightly reduced as time elapsed, and that its reduction rate increased as the air flow rate decreased. The simulation result seems to replicate these features. However, the simulation result could not replicate the immediate voltage drop, which emerged in case of 58 and 116 sccm flow rate. As mentioned in the previous section, this immediate voltage drop was trigged by the flushing event, which successively happens after the flooding develops in GFC. On the other hand, the simulation is not able to simulate the flushing event, because gases and liquid water in GFC well mixed and flow together without flooding in GFC. Thus simulation is not able to replicate the immediate voltage drop.

In case of 0.6 A cm^{-2}, experimental result showed that the dependence of the flow rate on cell voltage was large, and that the cell voltage decreased rather quickly within 15 min in the lower flow rate cases. The simulation result replicated these features qualitatively. Fig. 12 obtained by the simulation shows the liquid water saturation and oxygen gas density at cathode CL. In the case of highest flow rate of 232 sccm, water balance between accumulation and drainage seems to be acquired, resulting that the liquid saturation and the oxygen gas density reached constant value. On the other hand, the water in the case of smaller flow rate did not balanced, and then the liquid saturation and the oxygen gas density at cathode CL continuously increased and decreased, respectively. Namely the flooding in cathode GDL, especially near cathode CL, developed, and liquid water droplets hindered the oxygen transport in GDL, and then the cathode activation overpotential increased, resulting in the quick decrease of cell voltage shown in the experimental result.

Putting together the above consideration, it is understood that the immediate voltage change is triggered by flushing, and that it is not able to replicate with present our simulation. On the other hand, it is found that the relatively-slow voltage drop is caused by the flooding growth in GDL and CL, and that it can well replicate with our simulation.

5.2. Comparison of GFC image between simulation and experiment

Fig. 13 is the comparison of GFC images between the experiment and the simulation. Each image was taken at the time specified in Fig. 11. The simulation image expresses vapor density distribution with the highlighting where vapor is supersaturated or unsaturated. In the experiment image, the liquid droplet and fog are spread from the outlet to the upstream in

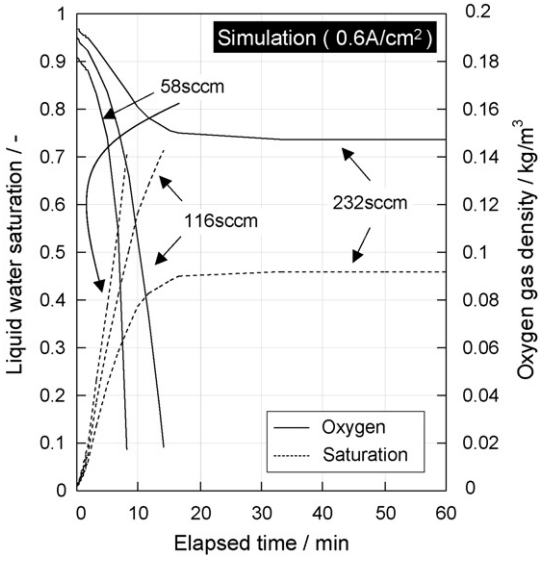

Fig. 12. Time variation of the liquid water saturation and the oxygen gas density at the cathode CL (the interface between PEM and cathode GDL) in case of 0.6 A cm^{-2}.

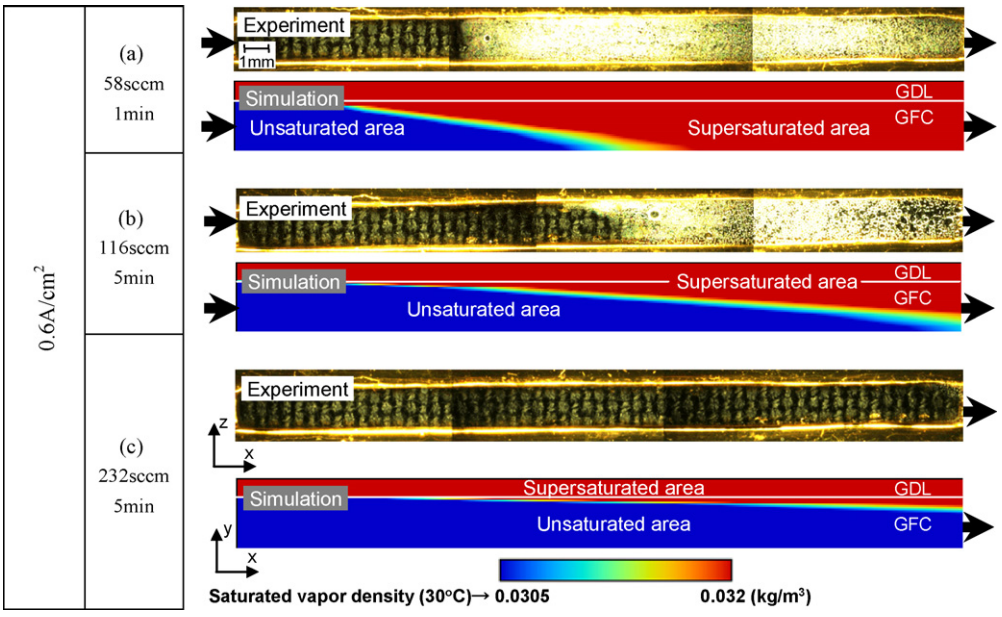

Fig. 13. Comparison between the cathode image and the vapor density distribution obtained by visualization experiment and numerical simulation, respectively.

GFC, and the region becomes larger as the air flow rate decreases. The simulation result seems to replicate these features, especially on the beginning point of the supersaturation region. Thus, it was confirmed that the observed fogging area corresponded to the supersaturated area in GFC.

6. Conclusion

We developed a two-phase flow and 2D simulator, where water transport at the interface of PEM/GDL and GDL/GFC was carefully treated. Numerical simulation was executed and compared with visualization experiment, reading to the following results. The Simulation could replicate the dependence of load current and flow rate on cell voltage. The simulation could also replicate the relatively-slow decrease of cell voltage, which was caused by the flooding in GDL and CL. Moreover, the simulation could replicate the supersaturation region in GFC and the flow-rate dependence of it.

Visualization experiment caught the immediate cell voltage change with liquid water film, which momentarily formed and covered GDL surface, synchronizing with the flushing-out of liquid water accumulated in GFC. This immediate voltage change with the dynamic water behavior was thought to be one of representative phenomena under flooding condition. Our simulation could not replicate this phenomenon, because of the use of well-mixed modeling in GFC.

References

[1] K. Tuber, D. Pocza, C. Hebling, J. Power Sources 124 (2003) 403.
[2] X.G. Yang, F.Y. Zhang, A.L. Lubawy, C.Y. Wang, J. Electrochem. Soc. 7 (11) (2004) A408.
[3] A. Turhan, K. Heller, J.S. Brenizer, M.M. Mench, J. Power Sources. 160 (2006) 1195.
[4] C.Y. Wang, P. Cheng, J. Heat Mass Transfer 39 (1996) 3607.
[5] Z.H. Wang, C.Y. Wang, K.S. Chen, J. Power Sources 94 (2001) 40.
[6] L. You, H. Liu, J. Heat Mass Transf. 45 (2002) 2277.
[7] M. Hu, A. Gu, M. Wang, X. Zhu, L. Yu, Energy Convers. Manage. 45 (2004) 1861.
[8] K. Ito, H. Masuda, T. Miyazaki, Y. Kakimoto, T. Masuoka, Investigation of flooding phenomena in PEMFC by two-phase flow numerical simulation, in: Proceedings of the Third International Conference on Fuel Cell Science, Engineering and Technology, Yipsilanti, USA, 2005.
[9] R. Taylor, R. Krishna, Multicomponent Mass Transfer, John Wiley & Sons, New York, 1993, pp. 79.
[10] K. Ito, N. Miyauchi, K. Onda, H. Koori, Inst. Electrical Eng. Jpn. Trans. 124 (3) (2004) 485.
[11] G. Lin, T.V. Nguyen, J. Electrochem. Soc. 153 (2) (2006) A372.
[12] S. Yamauchi, S. Sakuma, H. Nakatani, K. Mitsuda, Inst. Electrical Eng. Jpn. Trans. A 120 (5) (2000) 607.
[13] T.A. Zawodzinski, C. Derouin, S. Radzinski, R.J. Sherman, V.T. Smith, T.E. Springer, S. Gottesfeld, J. Electrochem. Soc. 140 (4) (1993) 1041.
[14] T.E. Springer, T.A. Zawodzinski, S. Gottesfeld, J. Electrochem. Soc. 138 (8) (1995) 2334.
[15] S.V. Patankar, Numerical Heat Transfer and Fluid Flow [Japanese Translation Version], Morikita Shuppan, Tokyo, 1983.
[16] K. Onda, T. Araki, T. Taniuchi, D. Sunakawa, K. Wakahara, M. Nagahama, J. Electrochem. Soc. 154 (2) (2007) B247.